Correlation between microstructure heterogeneity and multi-scale mechanical behavior of hybrid LPBF-DED Inconel 625

Noémie Martin, Anis Hor, Etienne Copin, Philippe Lours, Léon Ratsifandrihana

To cite this version:

Noémie Martin, Anis Hor, Etienne Copin, Philippe Lours, Léon Ratsifandrihana. Correlation between microstructure heterogeneity and multi-scale mechanical behavior of hybrid LPBF-DED Inconel 625. Journal of Materials Processing Technology, 2022, 303, pp.117542. 10.1016/j.jmatprotec.2022.117542 . hal-03596475

HAL Id: hal-03596475
https://imt-mines-albi.hal.science/hal-03596475v1

Submitted on 29 Aug 2022

Correlation between microstructure heterogeneity and multi-scale mechanical behavior of hybrid LPBF-DED Inconel 625

Noémie Martin[b,a,c,d,*], Anis Hor[b,a,c], Etienne Copin[b,a,c], Philippe Lours[b,a,c],
Léon Ratsifandrihana[d]

[a] CNRS, IMT Mines Albi, INSA, ISAE-SUPAERO, UPS, 3 rue Caroline Aigle, Toulouse 31400, France
[b] Université de Toulouse, Toulouse 31400, France
[c] Institut Clément Ader (ICA), IMT Mines Albi, INSA, ISAE-SUPAERO, UPS, 3 rue Caroline Aigle, 31400 Toulouse, France
[d] SEGULA Engineering, Immeuble EQUINOX - Bâtiment I, 24 Boulevard Déodat de Séverac, 31770 Colomiers, France

ABSTRACT

Keywords:
Hybridization
LPBF
DED
Inconel 625
In situ straining
Microstructure heterogeneity

The two additive manufacturing processes Powder Bed Fusion (LPBF) and Directed Energy Deposition (DED) have different geometrical resolutions and production flexibilities, making their hybridization attractive. LPBF microstructure displays fine grains, with weak preferential crystal orientation. DED generates a highly textured and inhomogeneous microstructure with equivalent grains diameters ranging from a few micrometers to over a millimeter. The microstructure of the hybrid LPBF-DED sample is the addition of these two microstructures with an interface free from cracks or particular pores. The effect of this strong heterogeneity of the hybrid microstructure on mechanical behavior is analyzed by tensile tests instrumented with local strain gauges, others using digital image correlation method and finally on samples tested inside a scanning electron microscope. This multi-scale characterization showed that the difference in the elastic properties causes the localization of the strain field and generates a plastic incompatibility at the interface. An optimized heat treatment leads to isotropic and homogeneous hybrid microstructure, with a larger DED grain size. It leads to identical plasticity mechanisms during tensile tests and lowers the strain gradient around the interface.

1. Introduction

The idea of combining additive manufacturing processes with other existing techniques or secondary processes is seen as an opportunity to bypass the limitations and expand the range of profitable applications for additive manufacturing (AM). Sealy et al. (2018) give an insight into the variety of existing combinations. Karunakaran et al. (2010) combined metal deposition and CNC machining to build dies with significant time and cost savings. Jones et al. (2012) demonstrated the feasibility and benefits of repairing turbine blades in an integrated additive and subtractive machine. The impact of such integrated machinery on the microstructure and mechanical properties of the material is also investigated by Feldhausen et al. (2021). These examples illustrate the attractivity of hybridization of AM and conventional machining to limit the AM drawbacks such as lower geometrical resolution and poor surface roughness. The state-of-the-art review paper by Webster et al. (2021) highlights that the hybridization of AM processes mainly concerns the combination with a secondary process, to control or improve the final properties (mechanical, geometrical, microstructural).

Soffel et al. (2021) shows interest in using additive processes to add features to conventional non-subtractive processes as well, such as casting, but combining various additive manufacturing processes is less commonly reported in the literature. The hybridization of LPBF and DED processes is starting to attract the attention of both industry and research. In the years 2010, examples with Ti6Al4V alloys for medical and aerospace applications emerged. Liu et al. (2016) targeted the satisfactory material properties and geometrical resolution characteristics of the LPBF process, while increasing the build volume as achievable by the DED process. They observed a good metallurgical bond at the interface, and tensile tests identified the DED material as the limiting factor of the overall resistance. Qin et al. (2019) confirmed that the DED is the limiting process, even after homogenizing heat treatment. Graf et al. (2013) demonstrated that combining the LPBF and the DED processes allows decreasing the production time of an integrated turbine blade significantly (>50%), as compared to manufacturing the part

---

* Correspondence to: Institut Clément Ader (ICA), Université de Toulouse, CNRS, IMT Mines Albi, INSA, ISAE-SUPAERO, UPS, 3 rue Caroline Aigle, 31400 Toulouse, France.

E-mail address: noemie.martin@isae-supaero.fr (N. Martin).

Nomenclature

AM	Additive Manufacturing
DED	Directed Energy Deposition
DIC	Digital Image Correlation
EBSD	Electronic Back Scattered Diffraction
El%	Tensile Elongation to failure
FCC	Face Centered Cubic
HT	Heat Treatment
KAM	Kernel Average Misorientation
LPBF	Laser – Powder Bed Fusion
SEM	Scanning Electron Microscope
TEM	Transmission Electron Microscope
UTS	Ultimate Tensile Stress
YTS	Yield Tensile Stress
ε%	Deformation in percent
σ	Stress in MPa

using LPBF solely. Their observations of the microstructures did not identify specific pores or cracks at the interface. Another opportune application by Oh et al. (2019) for LPBF-DED hybridization is the repairing of LPBF parts. The DED process parameters and the depth of the recharge deposit on LPBF 316 L stainless steel parts were found to influence the bonding at the interface. The tensile strength and elongation of repaired samples were found to decrease compared to full LPBF samples. It was assumed to be the result of the poor interface bonding. These studies were among the first to investigate the hybridization of LPBF and DED and prove its feasibility and effectiveness. The metallurgical and mechanical characterizations also established that DED material was the weakest link in terms of strength for the hybrid parts, but further investigations as to the role of the interface between the LPBF substrate and the DED deposition on the global behavior of parts were not conducted.

More recently, Godec et al. (2021) investigated more deeply the hybridization of LPBF and DED Inconel 718 for aerospace applications. A detailed investigation of the two microstructures produced was conducted. The difference in grain sizes, textures, and dislocation densities justify the better mechanical strength in LPFB. The heat-treated LPBF microstructure is completely homogenized, but some grains remained elongated in the DED microstructure. During the treatment, γ' and γ" secondary phases precipitated, as well as some undesirable δ phase in the DED material. These comparisons between LPBF and DED microstructures and mechanical properties are consistent with other studies reported in the literature such as Marchese et al. (2017) who compared LPBF and DED Inconel 625 separately. Godec et al. (2021) then tested heat-treated hybrid tensile samples. The tensile fracture was located in the DED material with mixed ductile and brittle failure mechanisms that were attributed to the δ phase precipitates. Further tensile tests on standard cylindrical samples instrumented with image correlation showed that the plastic deformation is concentrated in the DED material. The part of the hybrid sample made by LPBF barely reaches 1% of elongation before the sample rupture. The global mechanical behavior remains process-dependent despite the attempt to homogenize the microstructures by an annealing treatment.

In short, only three teams published results about mechanical behavior of hybrid LPBF-DED. These recent publications state that in a hybrid LPBF-DED part, the DED process is the limiting factor in terms of ultimate strength, due to its initial weaker characteristics. Similarly, the global ductility of a hybrid part is affected compared to a full-single process sample. However, to the author's best knowledge, except for the ultimate strength, the factors influencing the global behavior of a hybrid part are not identified. The identification and understanding of the influencing factors would allow to anticipate and control the behavior of a hybrid part, and particularly design post-treatment such as heat-treatments in accordance. This study seeks to fill this gap in the literature and identify the determining factors of the yield stress and deformation behavior of a hybrid LPBF-DED part. The study describes the difference in microstructures and mechanical behavior of the two halves of hybrid parts and identifies the main factors impacting the global mechanical behavior.

The tensile behavior of hybrid LPBF-DED Inconel 625 is investigated on the macro, meso, and micro scales, with a quantification of the deformation phenomenon the DED, the LPBF, and at the interface. The macroscopic characterization confirms statement found in the literature that the DED is the limiting factor in terms of ultimate strength. The mesoscopic mechanical characterization adds to the current literature knowledge by showing that the global yield stress of a hybrid part is determined by the gap between the yield stress of both materials, and not solely the weakest. Hence, a heat treatment reducing this gap is successful in obtaining a predictable behavior. The microscopic observations show that the transition zone between the two microstructures does not influence on the global tensile behavior. However, a homogenous microstructure, notably equiaxial grains, is beneficial to a homogeneous deformation.

2. Materials and Method

The metallurgical bonding of as-built and treated Inconel 625 LPBF-DED samples is characterized by SEM and optical observations. As-built and treated Inconel 625 hybrid LPBF-DED mechanical behavior is then studied, with a focus on the role of the interface. The global behavior is characterized by tensile tests on hybrid cylindrical samples instrumented with a global extensometer and local strain gauges. Then, flat tensile samples are monitored by digital image correlation (DIC) to assess the mesoscopic behavior and deformation. Finally, particular in situ tensile samples are tested within a SEM to relate the macroscopic behavior to the plasticity observed at the grain's scale.

2.1. Hybrid fabrications and heat treatment

Hybrid LPBF-DED samples have been built sequentially. First, vertical cylinders with a height of 50 mm and diameters of 12 mm and 20 mm were printed by LPBF on an SLM Solution 125 HL machine. The building plate used is stainless steel, with 5 mm support structures. After the building plate is removed from the building chamber and cleaned from any residual powder, the cylinders' height was completed up to 100 mm by DED deposition on the top layer of the LPBF construction, without further surface preparation. The DED machine used was a BeAM-AddUp modulo 400. It should be noted that no preheating of the LPBF cylinder substrate was applied before the DED processing.

Table 1 details the Inconel 625 powders' granulometry and chemical

Table 1
Granulometry and chemical composition of a) LPBF and b) DED powders used.

a) LPBF powder							
Powder size (deciles)	Chemical composition (wt%)						
D_{10} = 21 µm	**Ni**	**Cr**	**Mo**	**Nb+Ta**	**Fe**	**Co**	**Si**
D_{50} = 34 µm	Bal.	21.41	8.99	3.69	4.13	0.16	0.09
D_{90} = 54 µm	**Mn**	**Ti**	**Al**	**C**	**S**	**P**	
	0.03	0.05	0.04	0.03	0.001	0.005	
b) DED powder							
Powder size (repartition)	**Chemical composition (wt%)**						
	Ni	**Cr**	**Mo**	**Nb+Ta**	**Fe**	**Co**	**Si**
3% < 45 µm	Bal.	20.5	8.5	3.93	0.8	0.17	< 0.10
1% > 90 µm	**Mn**	**Ti**	**Al**	**C**	**S**	**P**	
	0.04	0.33	0.24	0.01	0.001	0.01	

compositions as given by the furnishers. The main difference between the two powders is the granulometry. The DED process requires a coarser powder than the LPBF process, due to the way it is conveyed. In terms of chemical composition, both powders are per the standard UNS N06625, which defines Inconel 625. Table 2 summarizes the standard process parameters used, based on the recommendations from the respective machine manufacturer.

The annealing treatment was determined by preliminary experimental observations. The objectives were to recrystallize and chemically homogenize both the LPBF and the DED microstructures while preserving their mechanical properties as much as possible. The optimal conditions determined were a holding of 4 h at 1150 °C in a pre-heated furnace, followed by a water quench.

Three different geometries of mechanical characterization samples were machined from these cylinders. Two of them were extracted from ø12mm cylinders: (1) cylindrical tensile samples given in Fig. 1a and (2) the flat In Situ SEM geometries given Fig. 1c. The third geometry was extracted from ø20mm cylinders: (3) flat tensile samples given on Fig. 1b. For all specimens, the DED-LPBF interface is localized at the center of the solicited section. In the following study, the parts of the hybrid samples made by the LPBF process and by the DED process are referred to as “LPBF zone” and “DED zone” respectively. The color-coding red for features concerning the LPBF zone and blue for the DED is respected throughout the paper.

The flat geometries (Fig. 1.b, c) are obtained in two steps illustrated in Fig. 2. Three strips are cut from one cylinder via Electric Discharge Machining and then cut to the desired shape. Notches permit to identify whether the strip is extracted from the center or the side of the cylinder.

2.2. *Microstructural observations*

The microstructure was investigated by optical and scanning electron microscopy. The samples were mechanically polished down to mirror finish and etched using Aqua Regia solution, 30 vol% HNO3 – 70 vol% HCl. Electron backscatter diffraction (EBSD) analysis was carried out using a JSM-7100 TTLS LV SEM equipped with an HKL EBSD system. The post-treatment of the data is done using the MTEX Libraries (Bachmann et al., 2011). Misorientations above angles of 10°, delineating a minimal grain area of 10 pixels (20 µm^2, or 2.5 µm equivalent diameter) are considered as grain boundaries. These parameters are in the range of the recommendations of the analytical work on FCC alloys by Brandon (1966), and are used in more recent studies of LPBF Inconel 625, such Marchese et al. (2020). The equivalent grain diameter (diameter of a disk with the same area as the grain) was considered for grain size analysis. Twin boundaries are determined as a misorientation of 60°+ / 5° twisted about the (111) plane, according to the initial work of Brandon (1966) and more recently validated in the work of Sangid et al. (2010). The twins are not considered for the calculation of the grain size.

Table 2 –
Process parameters used for the fabrication of a) LPBF b) DED parts.

a) LPBF parameters			
Energetic Parameters		Lasing Strategy Parameters	
Laser Power	275 W	Hatch Distance	0.12 mm
Laser Speed	760 mm/s	Hatch Stripe Length	10 mm
Layer Thickness	0.05 mm	Rotation Layer to Layer	67°
Building plate Temperature	200 °C		
b) DED parameters			
Energetic Parameters		**Strategy**	
Laser Power	900 W	Concentric circles	
Laser Speed	13 mm/s	from outer to inner circle	
Powder flow	9.5 g/min		
Spot Size	1.9 mm		
Delay between layers	21 s		

2.3. *Mechanical characterizations*

Vickers micro-hardness (mHV): indentation matrices of 6 columns spaced out by 1 mm and 10 lines spaced by 0.5 mm were performed on as-built and heat-treated hybrid samples. The first column is indented 1 mm away from the sample’s extremity to avoid side effects disruption. The matrix is manually situated so that the interface between LPBF and DED is at mid-height. The tested area represents a rectangle of 4.5 mm height by 5 mm length, corresponding to half a cylindrical sample of 12 mm diameter. The load applied on the 136° pyramid was 3 kg, and maintained 10 s for each indent. The Vickers hardness is then deduced from the diagonals.

Tensile tests with local strain gauges: these tests were done on three as-built and three heat-treated cylindrical samples on an axial Instron 5902 machine. The strain rate controlled tensile tests were performed until the sample’s failure with 10^{-3} s^{-1} strain rate. Each sample was instrumented with an optical extensometer that measures the global strain of the full effective gauge length. Two as-built and two treated samples were further instrumented with local strain gauges in both the LPBF and DED zones. They were glued to the surface of the cylindrical samples.

Tensile tests with DIC: these samples were instrumented with an optical extensometer and speckle paint for digital image correlation (DIC) analysis. The tests were strain rate-controlled with the optical extensometer. According to the NF EN 2002–001 standard, two strain rates were applied during the test. The rate 8×10^{-5} s^{-1} was imposed until a strain of 0.5%. Then, the strain rate was increased to 1.5×10^{-3} s^{-1} until failure. DIC images were recorded with two cameras at a 2 Hz acquisition rate during the test. The strain fields were computed using VIC3D software.

In situ SEM tensile tests: these tests were executed on a stroke-controlled Kammrath-Weiss 5 kN module from Eden Instrument installed in a Zeiss SEM. The in situ tensile tests were performed with a constant stroke rate of 2 mm/s. During loading, automated image capture was carried out at the frequency of 10 Hz. In addition, tests were occasionally paused at constant load levels to take further images manually at various magnifications. For better identification of the microstructure, samples were manually polished and slightly etched with *Aqua Regia* solution before the tensile tests.

3. Experimental results

3.1. *As-built and heat-treated microstructures of hybrid parts*

Optical and SEM observations of hybrid samples revealing the as-built LPBF and DED Inconel 625 microstructures in the vicinity of their interface are given in Fig. 3. The yellow lines delineate the melt pools and highlight the similarity of both DED and LPBF microstructures, but at different scales. Both display the typical hemispherical melt pools crossed by heterogeneously shaped and elongated grains. Moreover, a dendritic or cellular substructure with pronounced Nb- and Mo-rich chemical inhomogeneity in the interdendritic/intercellular spaces is detected in both LPBF and DED materials by the SEM chemical contrast mode, illustrated by Fig. 3b. Only the scales of those features differ. DED melt pools, grains, and dendrites are significantly larger than those of the LPBF material.

The interface between the DED and the LPBF is shown in Fig. 3a. It is neat and devoid of porosity or cracks and follows the undulations of the DED melt pools at the macro scale. The density of the hybrid samples is as satisfactory as the pure LPBF and pure DED, measured to be more than 99,9%. This suggests a good metallurgical bonding by sufficient remelting of the as-built LPBF top surface when adding the first DED layers. At a lower scale (Fig. 3b), SEM observations reveal a region at the interface marking the transition between the two microstructures (about 50 µm thick) marked in red in Fig. 3b, made of an intermediate microstructure between the large DED dendrites and fine LPBF dendrites.

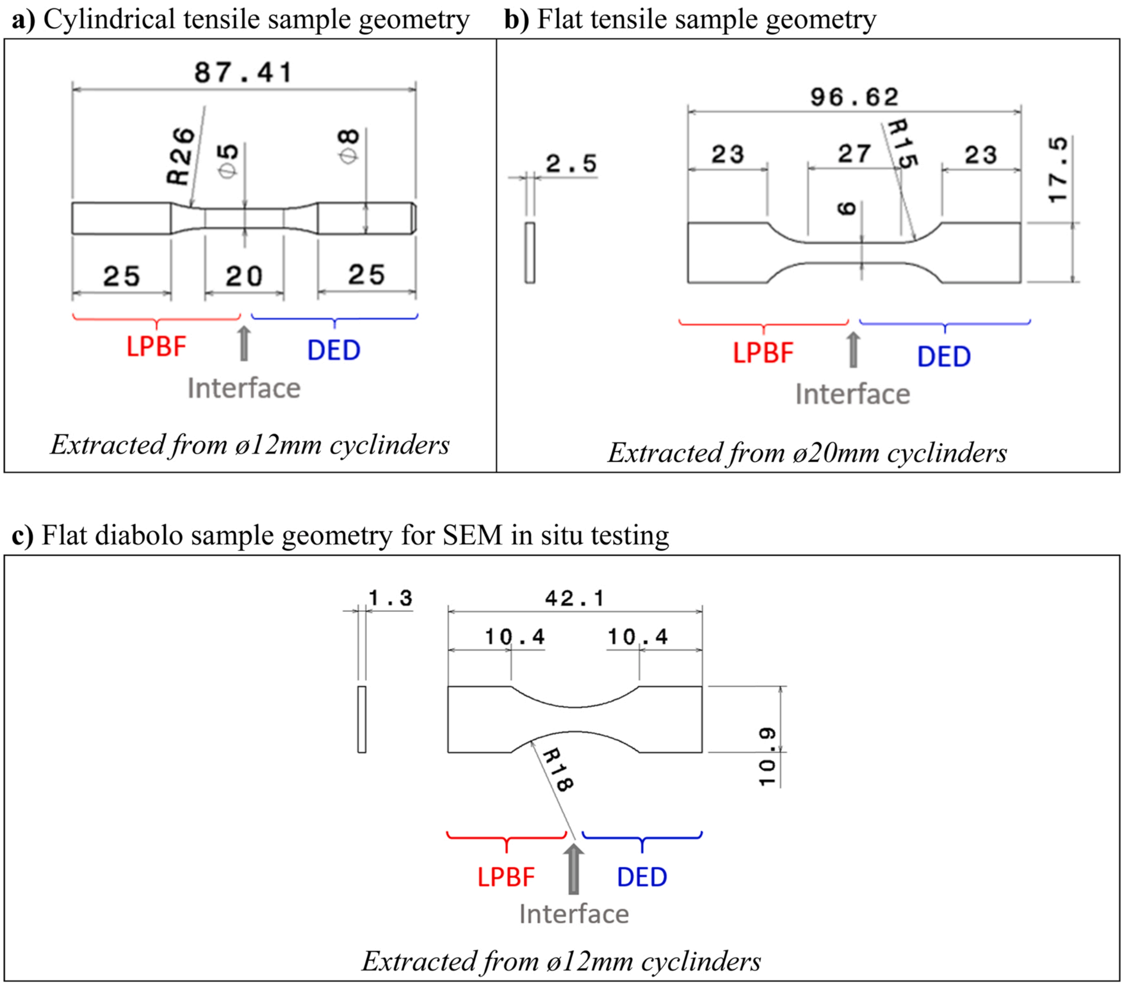

Fig. 1. Geometries of the mechanical characterization samples. Dimensions are given in millimeters.

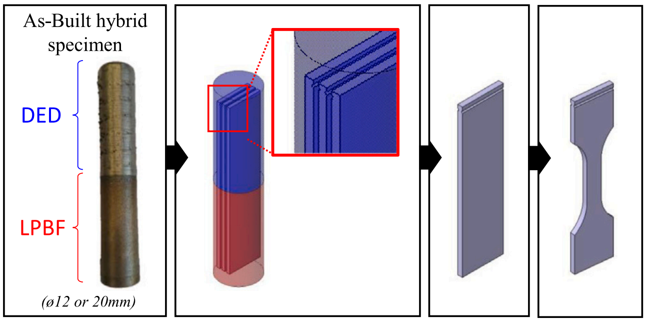

Fig. 2. Illustration of the extraction steps of flat samples from as-built cylinders.

More detailed insight into the grain structures is given by the EBSD inverse pole figures in Fig. 4. The LPBF process parameters and strategy used led to fine and elongated grains along the melt pools boundaries, with an average equivalent diameter calculated of 11 ± 7 μm. The crystallographic texture is weak, as shown in Fig. 4a and c. This microstructure is rather homogeneous at the sample scale in the LPBF part (Fig. 4a). On the other hand, the DED fabrication conditions induced more crystallographic texture and larger grains. The average equivalent diameter is 32 ± 38 μm, but some grains display equivalent diameters larger than a millimeter higher in the deposited cylinder (Fig. 4b). Unlike the LPBF microstructure, the DED microstructure is rather heterogeneous. Three distinct zones of similar width stand out in Fig. 4b: the center has fine grains, followed by a zone of about one third of the radius with very large vertical columnar grains, and epitaxial grains at the surface of the sample. The large grains induce a strong < 110 > texture along the vertical building direction. The orientation direction function reaches 8 on the sample's pole figures in Fig. 4b.

The observation of the interface by EBSD (bottom magnified inset in Fig. 4a) does not reveal a clear manifestation of the 50 μm thick zone observed by SEM between the DED and LPBF. However, a change in the grain shape from elongated to small and equiaxial put in evidence the delineation of the first layers of the DED deposition, indicated by black arrows on the right magnified inset in Fig. 4a.

Fig. 5 displays the Kernel Average Misorientation (KAM) image in the vicinity of the interface. The dislocation density can be approximated by this EBSD results, as in Fang et al. (2018) for LPBF Inconel 625. It is known that the sample's surface preparation steps such as polishing can alter the KAM measurement (Sánchez Camargo, 2019), but in the present case, the DED and LPBF Inconel 625 microstructures observations were drawn from the same sample, with the same polishing history. The density of misorientations appears to be much higher in the LPBF microstructure than in the DED microstructure.

The microstructures obtained after the 4 h heat treatment at 1150 °C are illustrated in Fig. 6. In both LPBF and DED regions, the microstructures are quite similar to that of conventional wrought Inconel 625: the LPBF and DED specific microstructures recrystallize into equiaxial grains with a high density of twins. The crystallographic texture observed in the as-built state also disappeared giving rise to a rather isotropic structure (Fig. 6a). The heat treatment and recrystallization

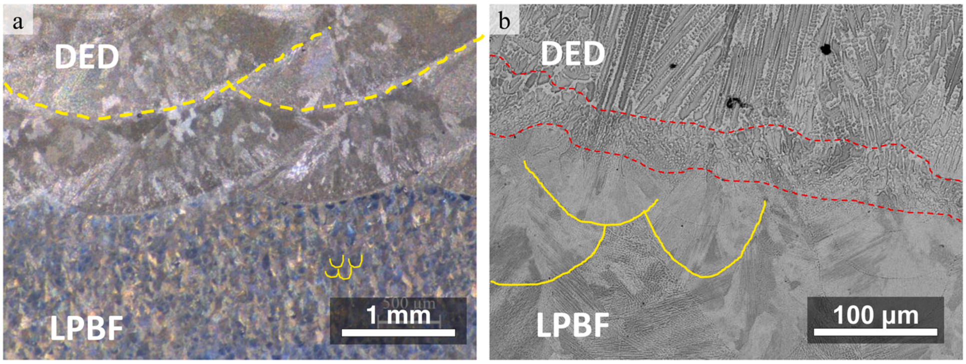

Fig. 3. a) Optical and b) SEM observations of hybrid LPBF - DED Inconel 625. (For interpretation of the references to colour in this figure, the reader is referred to the web version of this article)

process led to a significant increase of the average equivalent grain diameter, with still a large difference of scale between LPBF and DED: 33 ± 15 μm for the treated LPBF (against 11 ± 7 μm for the as-built) and 121 ± 90 μm for the treated DED (against 32 ± 38 μm for the as-built). The large standard deviations noted in the case of DED grain size are due to the presence of a few very large grains.

SEM observations confirmed that the dendritic structures in both LPBF and DED Inconel625 are fully homogenized by the heat treatments. The 50 μm thick transitional layer observed on the as-built hybrid samples is no longer visible at the interface.

3.2. *Micro-Hardness*

Micro-hardness measurements performed in the vicinity of the interface of as-built and heat-treated hybrid samples are displayed in Fig. 7. A clear difference in hardness is observed between the LPBF and the DED as-built microstructures. As-built LPBF displays a Vickers micro-hardness of 290HV against 230HV for the DED. It is consistent with the microstructures observed, larger grains and dendrites as well as lower dislocation density in the DED compared to the LPBF as-built microstructure. There seems to be a transition zone with intermediate hardness with a thickness of at least 0.5 mm that could correspond to the first DED layer's epitaxial grains. It must be kept in mind that.

After annealing treatment, the LPBF hardness is significantly decreased, from 290HV to 219HV. The DED softens to a lesser extent, from 230HV to 202HV. The hardness of the two materials is more homogeneous.

3.3. *Global tensile behavior*

Table 3 compares the global tensile characteristics of the as-built hybrid specimens (cylindrical geometry) with the ones of full as-built LPBF and DED Inconel specimens. The hybrid samples exhibit a tensile and ultimate strengths intermediate between those of DED and LPBF samples. However, their total elongation to failure is significantly lower than full LPBF or DED (27% vs. 39% for LPBF and 56% for DED). It should be noted that in all tests, failure occurred in the DED zone.

Fig. 8.a shows the tensile curves obtained for one hybrid sample. The strains of the LPBF zone (red) and DED zone (blue) are obtained by the local strain gauge. The stress is supposed to be homogeneous between the two zones and equal to the global stress of the sample (structure). They seem to follow quite well the global behaviors from full DED and LPBF samples (dashed curves). The fact that the strain gauges curves stop at 5% is only due to their adhesive failure that prevents further recording. The plot of the global behavior of the sample measured by the optical extensometer of the full gauge length, in black, lays between the full DED (dashed blue) and the full LPBF (dashed red) sample curve, including in terms of yield stress.

The temporal measures have been plotted in Fig. 8b. The strain gauge measuring in the DED and LPBF zones shows an inflection point, a sign of the onset of plasticity. For the DED, it occurs slightly below the LPBF (red double triangles). In the case of the global strain curve measured by the optical extensometer, in black, two inflection points are noted with black double triangles.

Tensile properties after the 4 h of treatment at 1150 °C are summarized in Table 4. After the annealing heat treatment (HT), the tensile strength of AM Inconel 625 decreases, while the ductility increases. These changes are significant for the LPBF HT microstructure that reached similar properties to the DED HT microstructure. The HT hybrid samples show similar yield stress and ultimate strength as the DED (weakest region of the two). However, the deformation to failure is once more significantly lower than those of full LPBF and full DED samples. Again, the failure systematically occurred in the DED region.

The corresponding tensile curves in Fig. 9 illustrate well the decrease of the gap between the mechanical properties of LPBF and DED Inconel 625 after heat treatment. The LPBF still has a slightly higher ultimate strength than DED, but the yield stress synonymous with the onset of plasticity occurs at a similar stress level. It can be noted that again the individual behavior of the DED and LPBF regions measured with local strain gauge remains almost identical to the behavior of full heat treated DED and LPBF samples (dashed lines). When looking at the temporal evolution of the strain (Fig. 9b), the global strain-stress curve does not show the double inflection points observed in the as-built material.

3.4. *Tensile behavior in the vicinity of the interface*

Four flat samples were extracted from the sides of two cylinders (columnar grains in the DED microstructure, see Fig. 4), and two from the centers (mixed columnar and fine grains in the DED microstructure, see Fig. 4). They all were tested. The global behavior and mechanical characteristics obtained in as-built and heat-treated states given in Table 5 are very close to the ones obtained for cylindrical samples (Section 3.3). The as-built samples have a YTS of 464 MPa (center) or 456 MPa (side) versus 455 MPa for the cylindrical samples, and 335 MPa or 347 MPa versus 364 MPa for the heat-treated samples respectively. For a given state of heat treatment, the YTS does not seem to depend on the geometry of the sample or the type of DED microstructure.

The ultimate strength of as-built flat samples is slightly below the one of the cylindrical samples (722 MPa for the center flat sample versus 805 MPa for the cylindrical), but they remain acceptable when considering the variability of the results. No obvious difference in behaviors between the center samples and side samples was noticed despite the differences in the as-built microstructures of the DED regions. However, this difference in microstructures might explain the variability in the as-built samples behaviors, since the repeatability is slightly increased after the homogenization and recrystallization treatment, as suggested by the better superimposition of the curves.

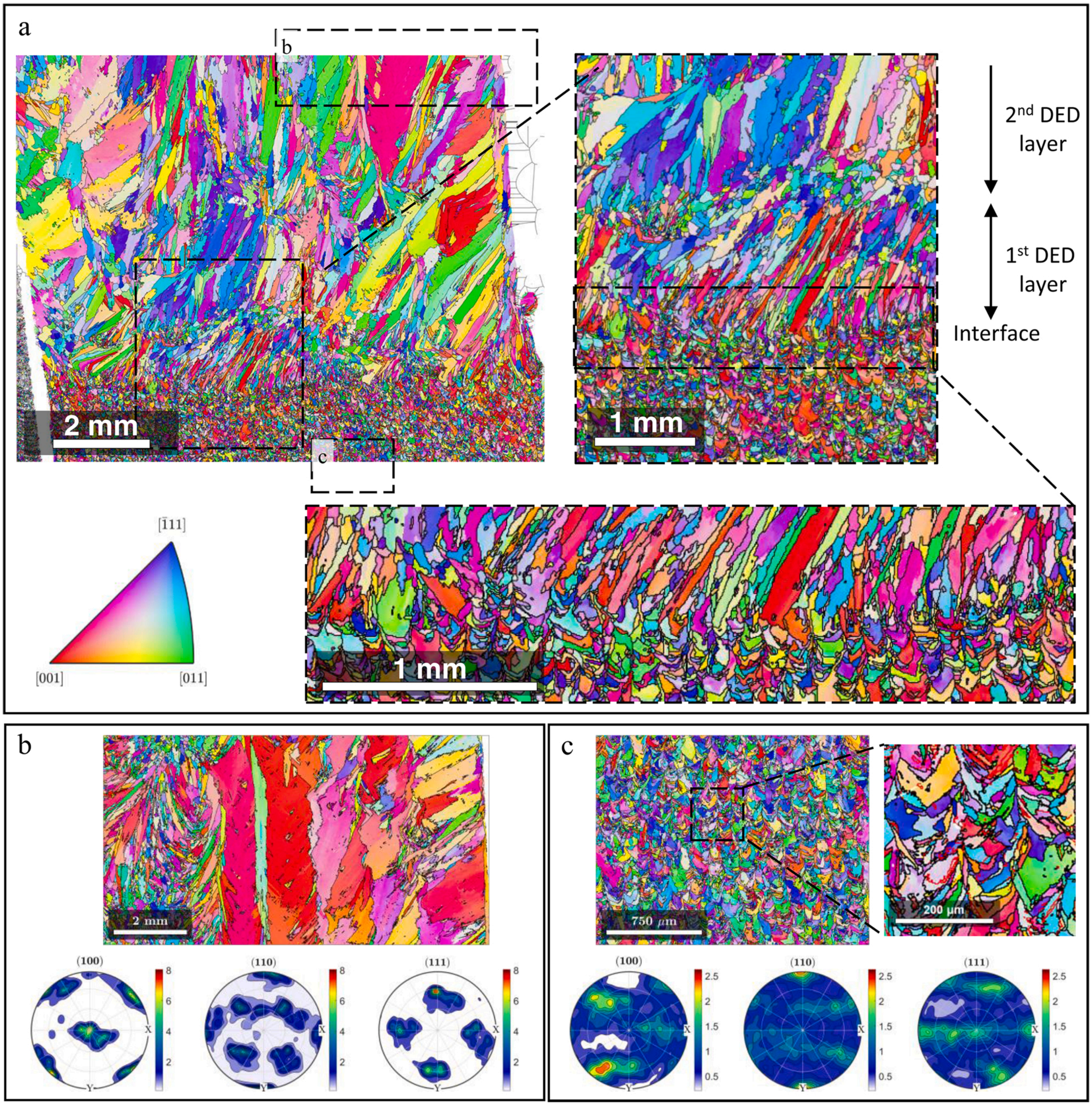

Fig. 4. IPF maps and pole figures a) hybrid LPBF-DED b) DED c) LPBF Inconel 625. (For interpretation of the references to colour in this figure legend, the reader is referred to the web version of this article.)

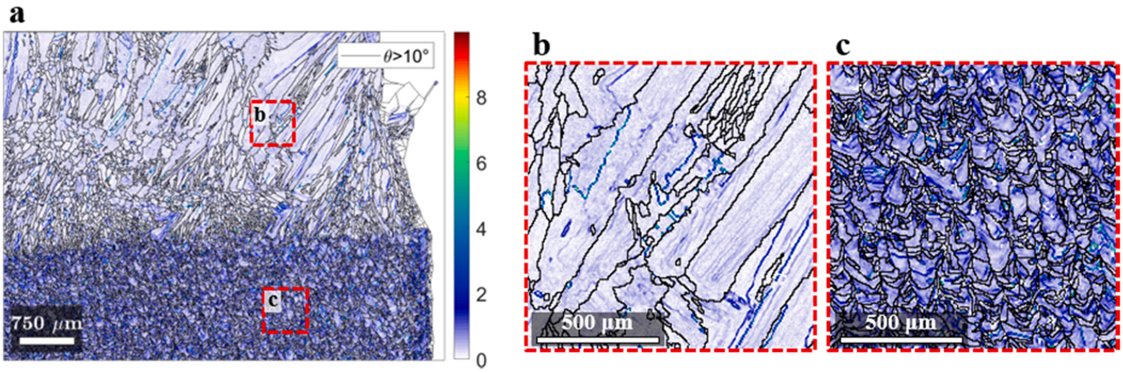

Fig. 5. a) Kernel Average Misorientation in an as-built hybrid LPBF-DED sample and details of the b) DED zone and c) LPBF zone.

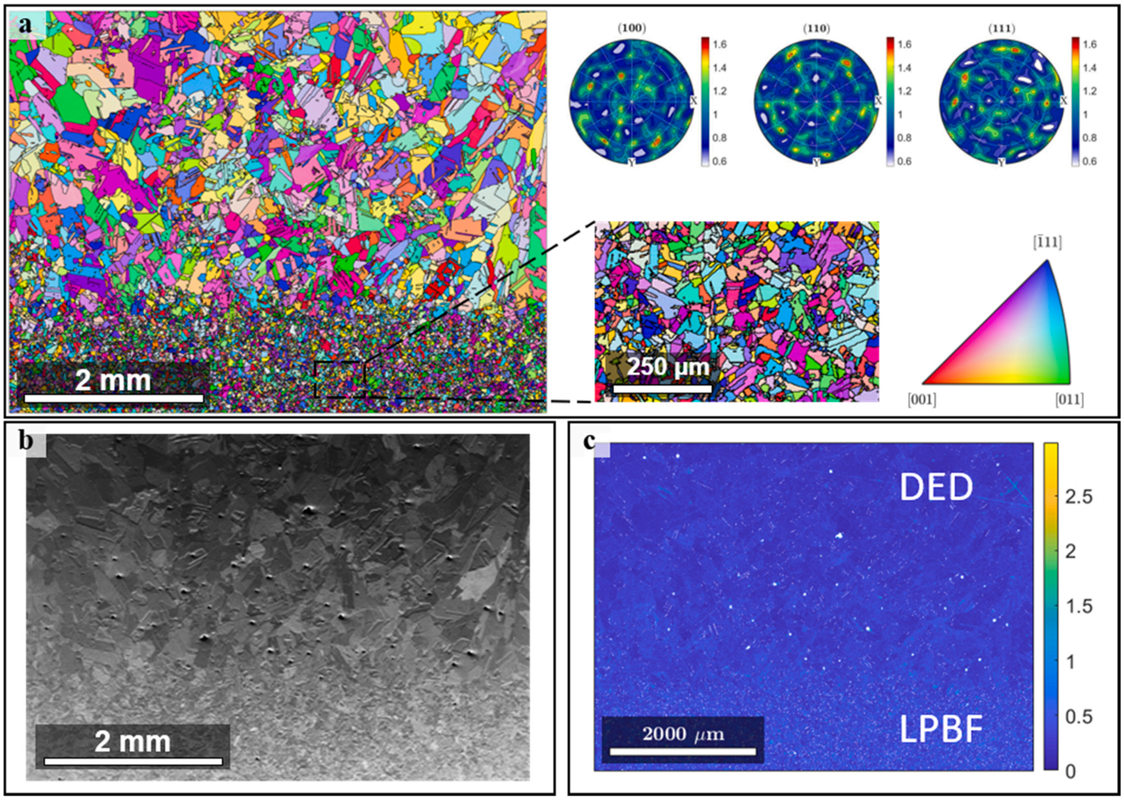

Fig. 6. a) IPF Z map of a treated hybrid LPBF-DED Inconel 625 sample b) SEM observation and c) Kernel Average Misorientation in an HT hybrid LPBF-DED sample.

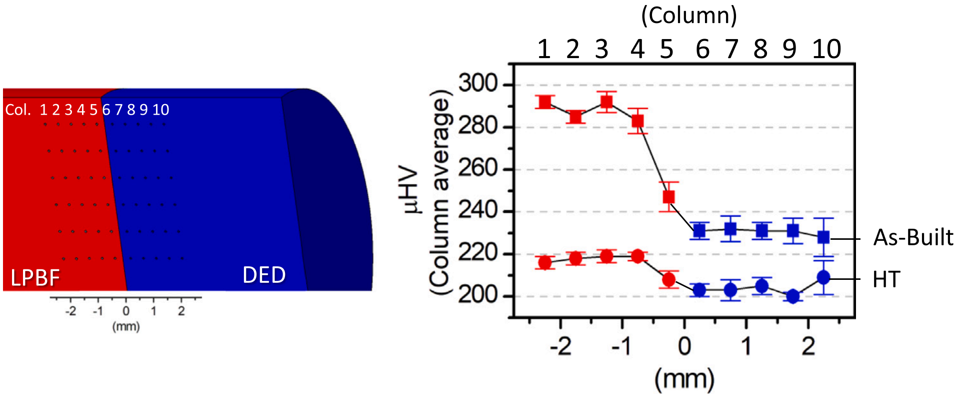

Fig. 7. Vickers micro-hardness results on as-built and heat-treated hybrid samples. The average of the 6 indents of each column is displayed with its standard deviation.

Table 3
Room temperature tensile properties of as-built Full LPBF, Full DED, and hybrid LPBF-DED Inconel 625.

	Full LPBF	Full DED	Hybrid LPBF-DED
YTS (MPa)	667 ± 3	420 ± 12	455 ± 9
UTS(MPa)	939 ± 1	779 ± 6	805 ± 13
ε (%)	39 ± 2	56 ± 2	27 ± 7

The digital image correlation (DIC) analysis is used to obtain the strain field evolution during tensile tests on flat samples. The evolutions of the strain fields for an as-built and a heat-treated flat sample are given in Fig. 10. Mean strains of LPBF and DED microstructures were extracted from DIC results using virtual linear extensometers in the DED and the LPBF zones. The stress is supposed to be homogeneous between the two zones and equal to the global stress of the sample (structure). The detection is less noisy than the optical extensometer, as there is no servo loop. Results correlate well with the experimental results obtained with the local strain gauges (Figs. 8 and 9). In the case of the as-built samples, Fig. 10a, a double inflection point of the global behavior is obvious with this type of monitoring. This is in agreement with the observations made previously with the cylindrical samples. Once treated (Fig. 10b), the double inflection point is no longer observed.

The evolution of the workhardening $\theta = d\sigma/d\varepsilon$ according to the true strain is plotted with the true tensile stress/strain curve on Fig. 10a.ii and b.ii for the as-built and the treated samples respectively. The double inflexion points on the global behavior of the as-built sample are visible also on the global workhardening curve. Two major changes in slope, corresponding to the start of workhardening for DED and LPBF. After the heat treatment, no such change in slope is observed.

The θ plots highlight that the workhardening in the DED starts for

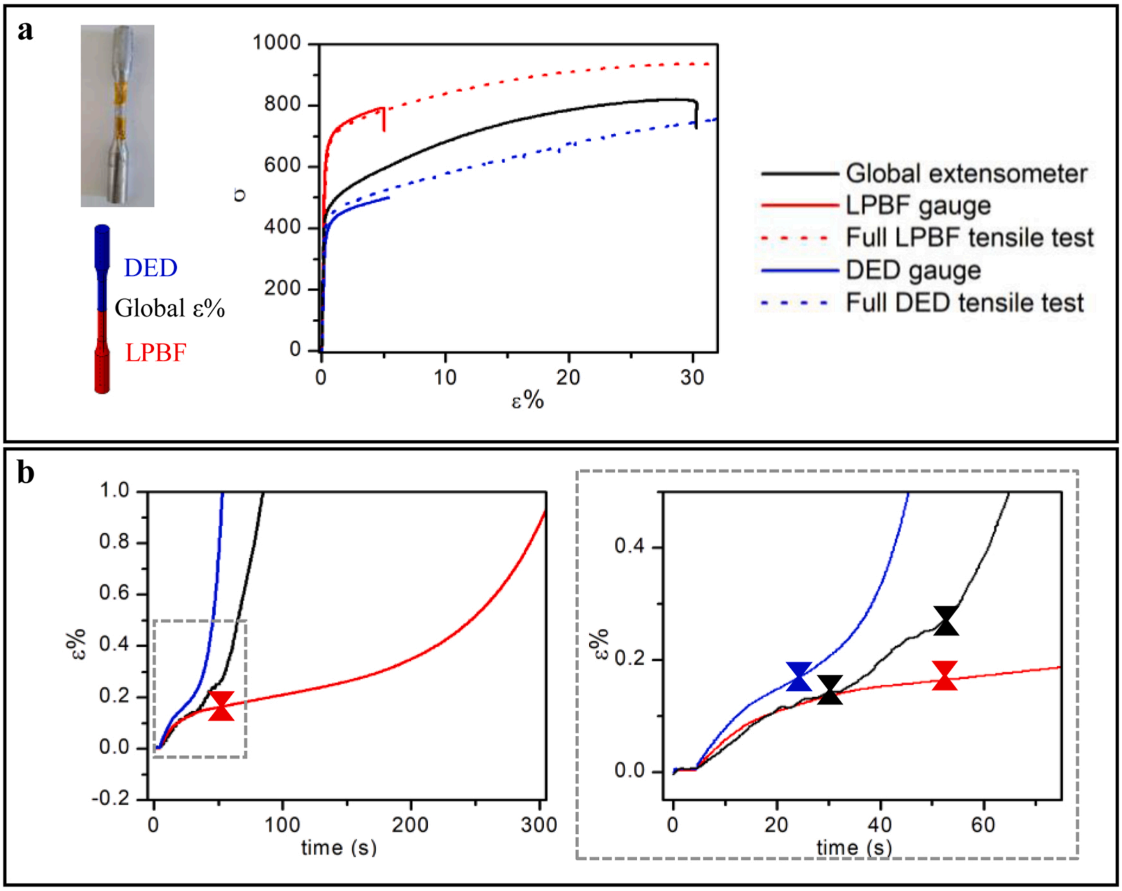

Fig. 8. a) Tensile curves of a cylindrical hybrid sample (black) equipped with local gauges on the DED (blue) and LPBF (red) zones, compared to full DED and LPBF samples (dashed). b) Measurements by the global extensometer (black) and local gauges (red/blue) relative to the testing time. (For interpretation of the references to colour in this figure legend, the reader is referred to the web version of this article.)

Table 4
Mechanical characteristics of annealed (4h1150°C) LPBF, DED, and hybrid Inconel 625.

	LPBF	DED	Hybrid
YTS (MPa)	363 ± 4	360 ± 14	364 ± 5
UTS(MPa)	853 ± 6	768 ± 1	762 ± 8
El (%)	62 ± 2	73 ± 2	44 ± 1

lower strain than in the LPBF, especially in the as-built state. For the treated samples, the workhardening plot confirm that both zones of the samples reach the onset of plasticity at the same global strain. The deformation in the sample is more homogeneous. It must be noted that the local gauges experience an adhesive failure slightly before 5% elongation, hence the workhardening coefficient calculated concerns only the beginning of the plastic flow. However, at 5%, the final values of the workhardening are very close between the LPBF and the DED, with the LPBF being slightly higher. The LPBF zone has a higher yield stress than the DED zone, and it experiences a slightly higher workhardening. Hence, in spite of the workhardening of the DED zone after

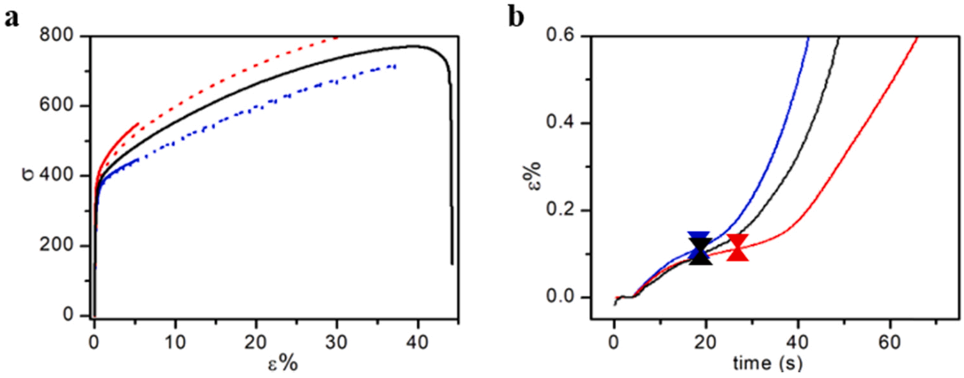

Fig. 9. a) Tensile curves of cylindrical hybrid treated samples (black) equipped with local gauges on the DED (blue) and LPBF (red) zones, compared to global full DED and LPBF treated samples (dashed). b) Measurements by the global extensometer (black) and local gauges (red/blue) relative to the testing time. (For interpretation of the references to colour in this figure legend, the reader is referred to the web version of this article.)

Table 5

Mechanical characteristics obtained from the tensile tests of flat hybrid specimens monitored by optical extensometer compared to cylindrical standard specimens.

	As-Built			Treated		
Sample type	**Flat Center**	**Flat Side**	**Cylindrical samples**	**Flat Center**	**Flat Side**	**Cylindrical samples**
DED grains	Fine	Columnar	*N/A*	Fine	Columnar	*N/A*
YTS (MPa)	464 ± 12	456 ± 11	455 ± 9	335 ± 1	347 ± 3	364 ± 5
UTS(MPa)	775 ± 3	785 ± 17	805 ± 13	722 ± 13	745 ± 6	762 ± 8
Curves	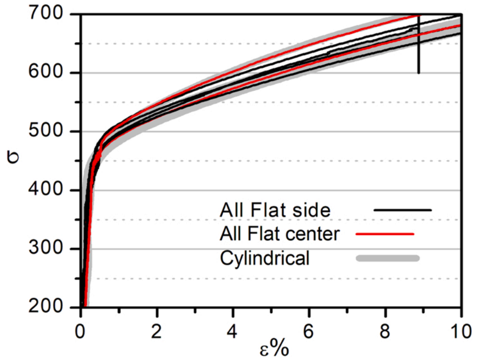			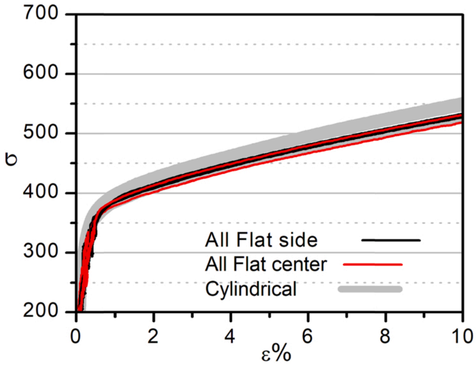		

the onset of plasticity, the local strain remains higher in the DED zone throughout the tensile test, and the difference is amplified.

The strain fields mapping in Fig. 10a.ii and b.ii illustrate the inhomogeneity of the deformation, and gap between the onsets of plasticity in the as-built sample. In the as-built sample, when the total elongation is at 0.8%, the deformation in the DED zone is plastic, with 1.5% strain on average. Simultaneously, the LPBF just reached 0.2%. It is only when the total elongation reaches 4.7% that the LPBF exceeds significantly 0.2%. Then, the DED is already elongated by 9.3%, and the gap never closes. The gradient between the LPBF zone, barely elongated, and the DED zone, which bears most of the elongation, is concentrated in just a few millimeters.

The annealed samples still display a difference in strain fields between the DED and the LPBF zones (Fig. 10.b). However, the plastic deformation of the LPBF zone starts for a lower total strain in the annealed hybrid samples than the as-built hybrid samples. Up to a total elongation of 0,2%, the strain is homogeneous in the sample. At 0,3%, the virtual extensometer in the DED zone is already at 0.7% strain, while the LPBF is just above 0.2%. Once both the DED and the LPBF zones are subject to plastic deformation, the gap between the elongation of DED and LPBF increases, as shown in Fig. 10b. The strain gradient at the interface is less marked, spread over just the few millimeters of the interface.

3.5. Local tensile behavior

In situ SEM tensile tests are performed to analyze the plasticity mechanisms of the as-built and HT in the vicinity of the interface of LPBF-DED hybrid samples. The observed phenomenons are associated qualitatively with a strain state.

Fig. 11 illustrates the different deformation steps for as-built samples extracted from the side and the center of the initial cylinders. All as-built samples display the same deformation mechanisms regardless of the zone of the cylinder from which they were extracted (side or center). Up to 1,5% approximated equivalent total strain, the microstructure remains the same. Later on, surface deformations are visible in the grains of the DED zone. The grains tilt, and what seems to be the different deposition layers boundaries become apparent. When comparing with the EBSD measurements given in Fig. 4, the correlation with the grains is obvious. As for the macro tensile samples, the failure systematically occurs on the DED zone, despite the diabolo geometry favoring the interface.

The failure in the DED zone initiates between layers (indicated by blue arrows), where smaller equiaxial grains were observed on Fig. 4. The crack does not initiate from the side of the elongated grains, but in the zone where grains boundaries are likely to be perpendicular to the loading direction. It suggests an inter-granular failure. The interface between LPBF and DED, marked in orange, does not display any particular deformation nor play a role in the failure. At a lower scale, occasional slip bands (indicated in red) are observed. They cross the dendritic structures without deviating but change direction from one grain to another. It confirms the influence of the crystallographic texture on the deformation behavior. Surface deformations are also observed in the LPBF zone at the end of the test, but they are less marked. No slip-bands were observed.

In situ micrographs at various deformation steps for as-treated specimens are shown in Fig. 12. As for the as-built samples, no difference in tensile behavior has been observed between the side and center annealed samples. The signs of plasticity are similar to the as-built material, with a grain-wise surface deformation. The DED deposition layer boundaries are not clearly identified, due to the recrystallization. The failure occurred in the DED region for all treated samples, but it was not possible to identify if the former deposition layer boundaries had any effect.

At a lower scale, slip bands are more easily spotted, and twin boundaries are highlighted by their change in direction. It is noted that the deformation is more homogeneous between the LPBF and DED microstructures, even if plasticity is more obvious in the DED region.

4. Analysis and Discussions

4.1. Hybrid DED-LPBF Inconel 625 microstructures

The microstructures of the LPBF and DED zones in a hybrid sample are consistent with observations of full LPBF and full DED samples, and consistent with results from the literature. Marchese et al. (2017) compared LPBF and DED Inconel 625, and confirmed they are both multi-scale microstructures, organized in melt-pools with elongated

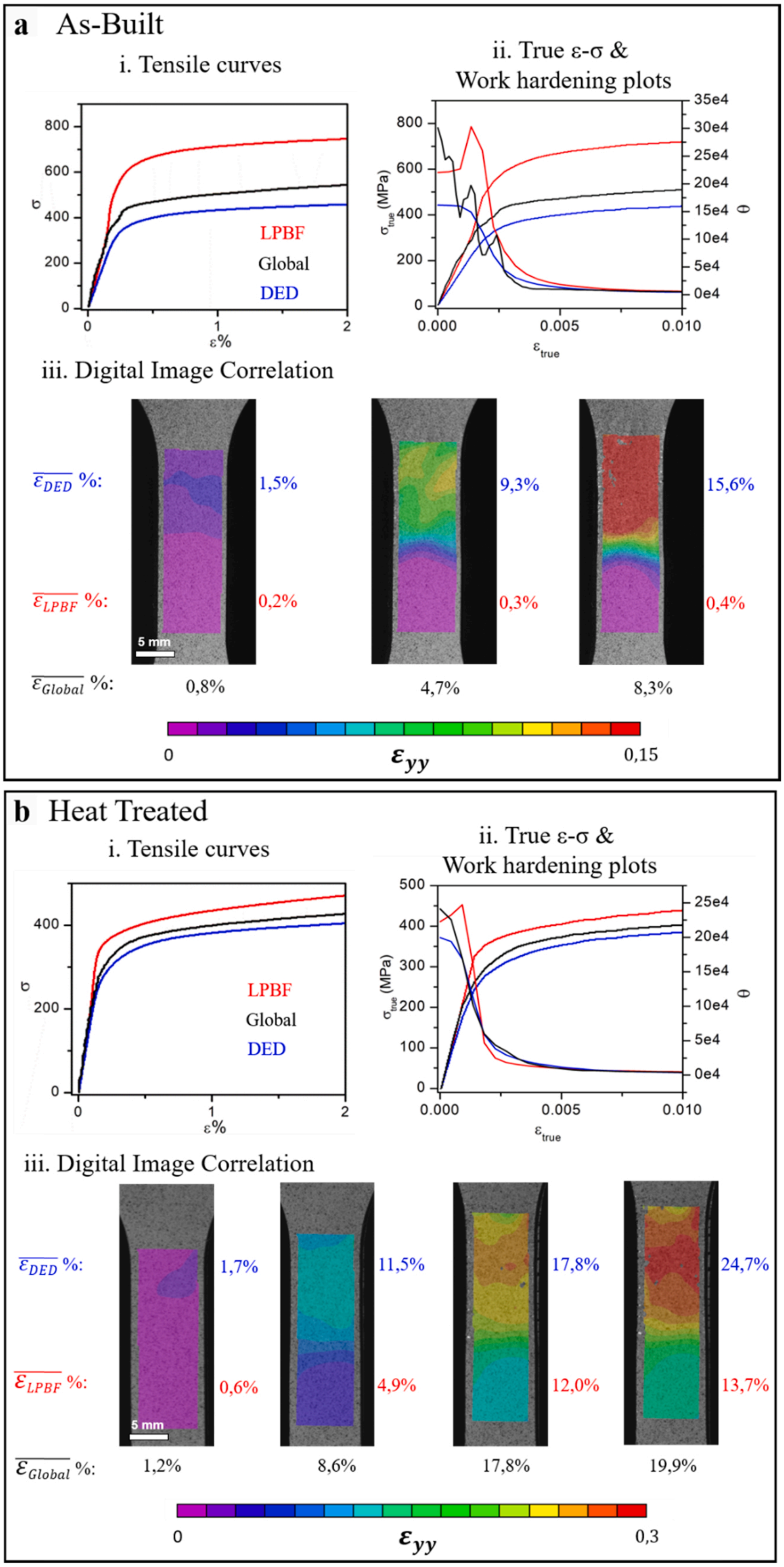

Fig. 10. Vertical strain fields mapping and tensile curves extracted from virtual linear extensometers of a) As-built flat sample b) Annealed HT flat sample.

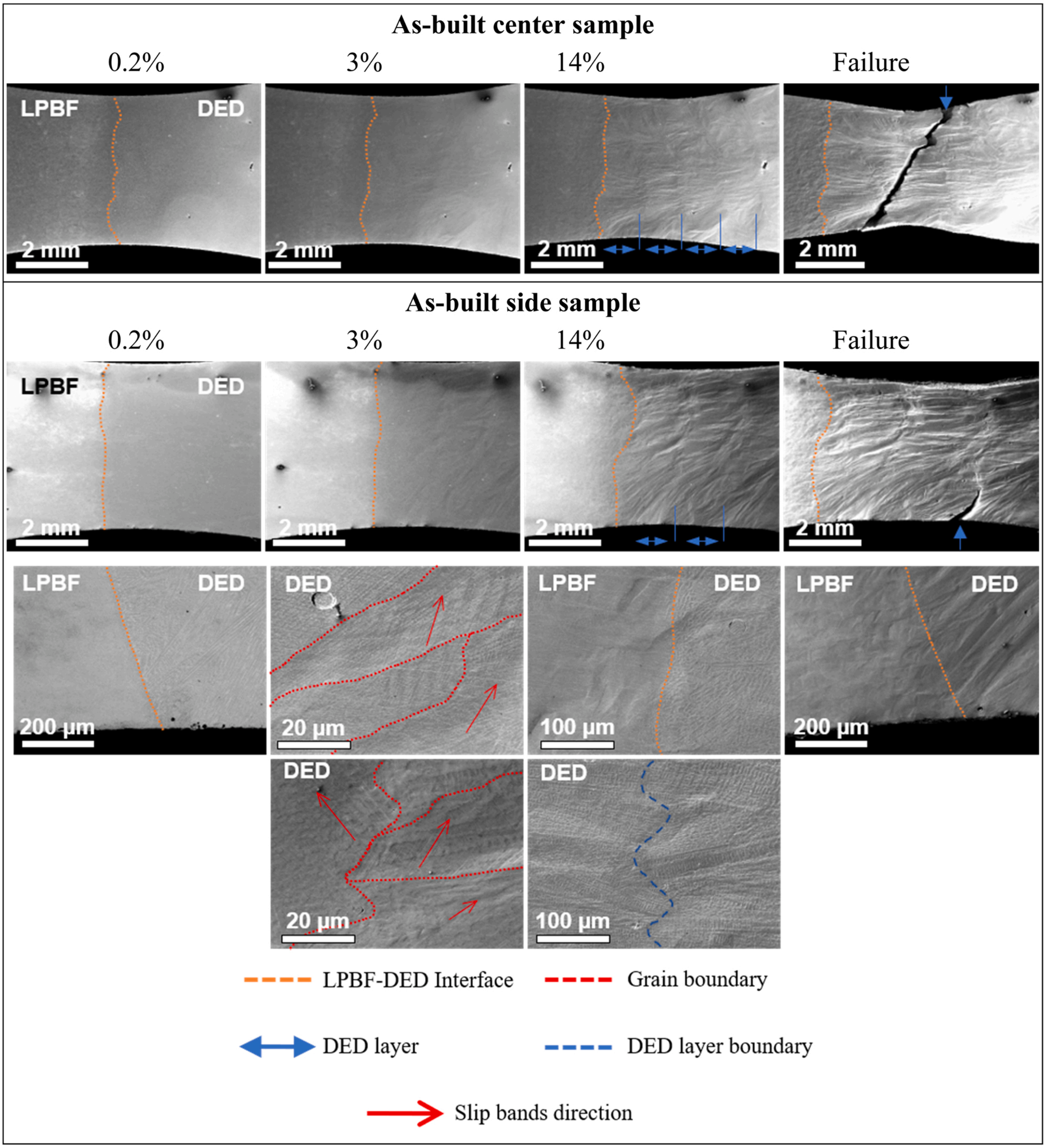

Fig. 11. SEM images of In situ as-built LPBF-DED tensile samples at various strain levels.

grains and dendritic substructures but with larger characteristic sizes in the DED. Dinda et al. (2009) observe the same microstructure in DED Inconel 625, and Sateesh et al. (2014) in LPBF, just to name a few. It is however known in AM that crystallographic features, such as the size of the grains, of the dendrite/cells, and the texture, vary according to the building parameters and strategy used. These building conditions influence the thermal gradients, and solidification and cooling rates that ultimately define the microstructure. For example, Marchese et al. (2020) and Li et al. (2017) obtain an LPBF Inconel 625 with columnar grains and marked texture, while Poulin et al. (2018) have a crystallographic structure similar to this study's, with grains shapes according to the melt pools, and weak texture. For the DED process, the grains' size, shape, and orientations have shown dependence on the strategy (Dinda et al., 2009). Ma et al. (2017) showed that they also depend on the sample's geometry and even on the location within the sample.

In this study, Fig. 4c shows that the DED deposition does not influence the microstructure of the LPBF substrate. It remains identical to the full LPBF sample. A weak crystallographic texture, with grain size and shape strongly correlated to the melt pools size and geometry. However, the specific DED columnar grains start to be generated following the third layer of DED deposition only. This can be due to the heat conduction through the LPBF substrate, initially at room temperature. After the first two layers, the substrate is at a higher temperature, hence decreasing the gradient of temperature, slowing the solidification, and

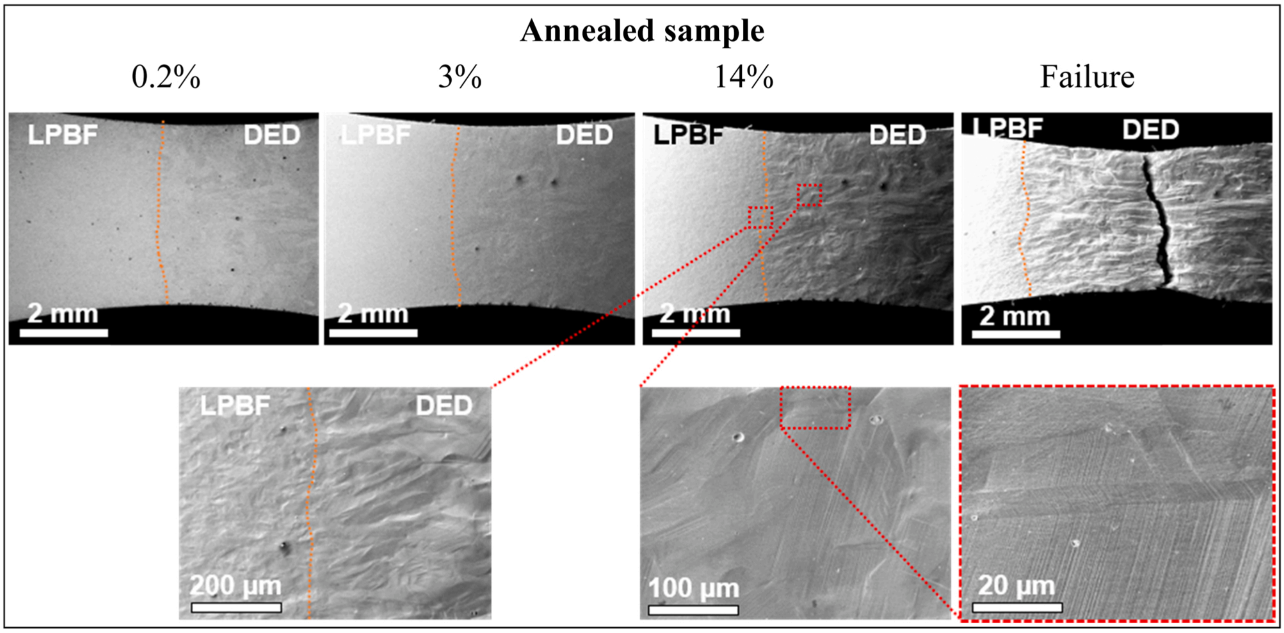

Fig. 12. SEM images of in situ annealed HT LPBF-DED tensile sample at various strain levels.

consequently decreasing the cooling rate. The columnar grains then grow, which is coherent with the results from Ma et al. (2017). In the LPBF substrate, despite a layer of 50 μm depth immediately below the first DED deposition layer where a mix of fine and coarse dendrites are found, the microstructure is identical to a full LPBF sample.

At a lower scale, the localized and high cooling rates of the processes LPBF and DED induce dislocations in the printed parts. TEM observations by Voisin et al. (2021) showed that the dislocations in LPBF 316 L steel are organized in cells, overlaid with the dendritic structure. Godec et al. (2021) confirmed the organization of the dislocations in cell substructures in LPBF Inconel 718, but no particular organization was observed in the DED Inconel 718 despite a significant dislocation density. This high dislocation density and its organization are held responsible for the high mechanical properties of additively manufactured materials (Li et al., 2021; Voisin et al., 2021). Hu et al. (2018) suggest that the dislocation cells should be considered as the grain boundaries and thus can explain the excessive hardening phenomenon in LPBF materials. In this study, the dislocation density is approximated by the Kernel Average Misorientation (KAM). The resolution of the measure does not permit quantifying or comment on the network of the dislocations. However, the observation of the hybrid sample in Fig. 5 confirms that the LPBF process induces a more significant dislocation density than the DED process for Inconel 625. The average intra-granular misorientation is constant in the LPBF zone (Fig. 5a and b), and higher in average than in the DED. The DED presents a low average misorientation, but low-angle grain boundaries from localized linear misorientations (Fig. 5c).

The observations of the hybrid samples highlight the successful production of good metallurgical bonding between the microstructures of DED and LPBF Inconel 625. No cracks or specific pores were observed, despite the absence of any specific surface preparation prior to the DED processing (as-LBPFed top surface). The crystallographic structure of the LPBF subtract remains unaltered, and the DED deposit becomes identical to a full DED sample after only 3 layers.

4.2. *Deformation heterogeneity between LPBF and DED microstructures*

The tensile tests performed on cylindrical samples and on flat samples revealed the same global behaviors. The hybrid samples have a conventional yield tensile stress of 455 MPa, below that of full LPBF (667 MPa) but above that of full DED (420 MPa). Locally, the DED and LPBF zones have the same behavior as the samples made entirely with the respective process. This heterogeneity influences global behavior.

In Fig. 8b, the as-built global behavior curve displays two inflection points indicated by the double black triangles. The DED and LPBF strain gauges curves have each only one inflection point, indicated by the double triangles in Fig. 8b. This inflection shows the change in response to the solicitation, marking the onset of plasticity. These inflection points do not happen at the same time for the LPBF and the DED zones during the tensile test. Due to the difference in local YTS (667 MPa for LPBF and 420 MPa for the DED), the DED plasticizes at lower stress, before the LPBF (Fig. 8b). The stress increases with the work hardening of the as-built DED microstructure until it reaches the YTS of the as-built LPBF microstructure. At this stress, the inflection point due to the onset of plasticity of the LPBF microstructure is detected by the LPBF gauge, indicated by the double red triangles in Fig. 8b. It causes the second inflection point in global behavior. Tensile tests with DIC showed similar results. The DED zone displays a total strain of approximately 9.3% before the LPBF zone reaches 0.3%, and its plastic deformation starts.

The lower elongation at failure observed on the hybrid samples (Tables 3 and 4) can also be explained by this inhomogeneity. The plasticity of LPBF starts only when the stress exceeds 667 MPa, corresponding to roughly 9% global strain. Hence the first 9% strain is mainly borne by the plasticity of the DED microstructure. The elongation of the sample is mostly situated in the DED zone. The local strain is significantly higher than the total strain measured by the extensometer. The failure occurs when the DED zone has reached an ultimate elongation similar to the ultimate elongation of a full DED sample. Observations confirmed no obvious deformation of the LPBF zone compared to the DED zone.

It is important to note that the interface between the DED and LPBF regions does not play any role in the tensile behavior and failure of the hybrid specimen. The failure occurs systematically in the DED zone, and no particular deformation is observed at the interface between the two processes during standard or in situ tensile tests. The DED microstructure is responsible for most of the ductility but is limiting in terms of the strength of hybrid material (lowest YTS and UTS). At a given solicitation, some regions experience locally higher levels of plastic deformation. The tensile strength of hybrid LPBF-DED Inconel 625 samples is at least equivalent to the DED and all samples failed in the DED zone. This is consistent with the lower ultimate strength obtained during the tensile tests performed on full DED samples and with literature. However, the global ductility of the sample is lowered due to the high difference in characteristics between as-built Inconel 625 obtained by the two processes.

4.3. Microstructure and tensile response after annealing heat treatment

The annealing heat treatment is generally applied to obtain a homogeneous microstructure from AM Inconel 625. Marchese et al. (2018) showed that 2 h at 1150 °C was required to recrystallize their as-built LPBF Inconel 625. Dinda et al. (2009) recommended 1 h at 1200 °C for their DED Inconel 625. In this study's case, as-built LPBF, DED, and Hybrid LPBF-DED samples were fully recrystallized with an annealing treatment of 4 h at 1150 °C. This heat treatment was optimized in a previous study. The annealed microstructure obtained is consistent with the same literature, with equiaxial grains, weak crystallographic texture, and a high twin density. The dislocation density estimated by the KAM appears to have decreased and is constant throughout the hybrid sample. It suggests the dislocations cells specific to the LPBF zone have been dissolved during the treatment, as shown in the literature. Voisin et al. (2021) show that the dislocations cells structures in LPBF 316 L stainless steel are dissolved following 1 h holding at 1200 °C, and with Godec et al. (2021) who showed the same in Inconel718 after 1 h at 1100 °C. The grain shape obtained after heat treatment is close to that of conventional Inconel 625 in both DED and LPBF processes, although a scale factor of roughly 4 remains between the grain's average equivalent diameters of HT LPBF and HT DED. This difference is inherited from the initial microstructures.

This quasi-homogenized microstructure affected the tensile deformation compatibility of hybrid LPBF-DED microstructures. The global behavior of the annealed heat-treated microstructure is similar to a homogeneous sample. The onset of plasticity in the LPBF zone is quasi-simultaneous with the onset in the DED regions in the cylindrical samples in Fig. 9. This leads to a single inflection point on the global strain-stress curve. The DIC method applied during the tensile tests of the flat samples confirms that despite the higher remaining strain in the DED zone throughout the test, it is more homogeneous. On the as-built samples, the LPBF strain was at 0,4% when the DED strain was already at 15%. After the annealing treatment, when the DED strain is at 15%, the LPBF is at 11%. In addition, the strain gradient at the interface is significantly lowered.

The deformation mechanisms identified by the in situ SEM tensile tests mostly occur through the formation of slip bands inside the grains. The slip bands follow preferential crystallographic planes, showing different directions according to the grain's orientations. In the case of the as-built DED, each grain becomes visible in Fig. 11, with its elongated shape aligned with the building direction, as the EBSD measurements in Fig. 4 show. The delimitations of the layers are easily spotted at the tip of those grains. It permits to identify that the failure occurs mostly at the boundary between two layers. It must also be noted that the similarity between side samples and center samples can be explained by this inter-layer failure. The inhomogeneous DED microstructure with large columnar grains is higher in the DED zone.

After annealing heat treatment, the deformation mechanisms remain the same, as emphasized by the tensile in situ SEM tests shown in Fig. 12. Yet, the slip bands are more marked. Their direction is more random too, as the texture is less pronounced. In addition, the presence of twin boundaries deflects the slip bands. The as-built samples showed only occasional plastic deformation on the LPBF microstructure, consistent with the observations on the macroscopic scale, but after the annealing HT, indications of plasticity are significant in LPBF too.

In conclusion, annealing heat treatment homogenizes the microstructure and the response to tensile loading. The deformation mechanisms of annealed LPBF and DED Inconel 625 become more similar. Despite a large difference in grain size, the compatibility of the deformation at the interface is ensured.

5. Conclusions

The multi-scale investigation of the hybrid LPBF-DED Inconel 625 samples highlighted the correlation between the microstructures obtained by the two processes and their mechanical behaviors. The importance of an annealing treatment is emphasized as it is prone to homogenize the microstructure of hybrid parts. This results in the homogenization of the tensile loading response of hybrid parts. The main conclusions can be summarized as follow:

- DED deposition with standard parameters of Inconel 625 on an as-built LPBF Inconel 625 substrate leads to good metallurgical bonding, without specific defects despite the absence of surface preparation.
- The global tensile strength of hybrid LPBF-DED Inconel 625 is intermediate to that of DED and LPBF Inconel 625. However, local plasticity can occur in the DED microstructure while the global behavior of the hybrid sample seems elastic. Strain at the failure of the hybrid sample is lower due to this inhomogeneous deformation.
- The applied annealing heat treatment leads to isotropic, recrystallized, homogeneous, and equiaxed microstructures in both LPBF and DED Inconel 625, with a larger DED grain size. It leads to identical plasticity mechanisms and lowers the strain gradient in the vicinity of the interface.
- DED is the limiting factor in terms of ultimate strength regardless of the heat treatment. The failure seems to occur at the boundary between DED layers in the as-built state. After the annealing heat treatment, the failure is still located in the DED region. The LPBF-DED interface plays no role in the tensile monotonic resistance with or without heat treatment.

Finally, to validate the compatibility of the two processes, further investigation in fatigue design at service temperature and fatigue are to be conducted in future work. Indeed, the strain gradient observed at the interface may have a specific influence under cyclic solicitations.

CRediT authorship contribution statement

Noémie Martin: Conceptualization, Methodology, Validation, Formal analysis, Investigation, Writing – original draft, Visualization. **Anis Hor:** Writing – review & editing, Methodology, Visualization, Supervision. **Etienne Copin:** Writing - review & editing. **Philippe Lours:** Writing – review & editing, Supervision. **Léon Ratsifandrihana:** Writing – review & editing, Supervision, Funding acquisition.

Declaration of Competing Interest

The authors declare that they have no known competing financial interests or personal relationships that could have appeared to influence the work reported in this paper.

Acknowledgments

This work was financially supported by Segula Technologies and Industrial Agreement of Training through Research, a public-private partnership (CIFRE). The authors would like to thank the I2M laboratory (Institut de Mécanique et d'Ingénierie – Bordeaux) for implementing the in situ SEM tensile tests.

References

Bachmann, F., Hielscher, R., Schaeben, H., 2011. Grain detection from 2d and 3d EBSD data-Specification of the MTEX algorithm. Ultramicroscopy 111, 1720–1733. https://doi.org/10.1016/j.ultramic.2011.08.002.

Brandon, D., 1966. The structure of high-angle grain boundaries. Acta Met. 14, 1479–1484. https://doi.org/10.1016/0001-6160(66)90168-4.

Dinda, G.P., Dasgupta, A.K., Mazumder, J., 2009. Laser aided direct metal deposition of Inconel 625 superalloy: Microstructural evolution and thermal stability. Mater. Sci. Eng. A 509, 98–104. https://doi.org/10.1016/j.msea.2009.01.009.

Fang, X.Y., Li, H.Q., Wang, M., Li, C., Guo, Y.B., 2018. Characterization of texture and grain boundary character distributions of selective laser melted Inconel 625 alloy. Mater. Charact. 143, 182–190. https://doi.org/10.1016/j.matchar.2018.02.008.

Feldhausen, T., Raghavan, N., Saleeby, K., Love, L., Kurfess, T., 2021. Mechanical properties and microstructure of 316L stainless steel produced by hybrid manufacturing. J. Mater. Process. Technol. 290, 116970 https://doi.org/10.1016/j.jmatprotec.2020.116970.

Godec, M., Malej, S., Feizpour, D., Donik, Balažic, M., Klobčar, D., Pambaguian, L., Conradi, M., Kocijan, A., 2021. Hybrid additive manufacturing of Inconel 718 for future space applications. Mater. Charact. 172. https://doi.org/10.1016/j.matchar.2020.110842.

Graf, B., Ammer, S., Gumenyuk, A., Rethmeier, M., 2013. Design of experiments for laser metal deposition in maintenance, repair and overhaul applications. Procedia CIRP 11, 245–248. https://doi.org/10.1016/j.procir.2013.07.031.

Hu, Y.L., Lin, X., Zhang, S.Y., Jiang, Y.M., Lu, X.F., Yang, H.O., Huang, W.D., 2018. Effect of solution heat treatment on the microstructure and mechanical properties of Inconel 625 superalloy fabricated by laser solid forming. J. Alloy. Compd. 767, 330–344. https://doi.org/10.1016/j.jallcom.2018.07.087.

Jones, P., Mcnutt, P., Tosi, R., Perry, C., Wimpenny, D., 2012. Remanufacture of turbine blades by laser cladding, machining and in-process scanning in a single machine. In: Proceedings of the Twenty Third Annu. Int. Solid Free Fabr. Symp., pp. 821–827 doi: 10.1016/j.phpro.2012.10.051.

Karunakaran, K.P., Suryakumar, S., Pushpa, V., Akula, S., 2010. Low cost integration of additive and subtractive processes for hybrid layered manufacturing. Robot. Comput. Integr. Manuf. 26, 490–499. https://doi.org/10.1016/j.rcim.2010.03.008.

Li, C., White, R., Fang, X.Y., Weaver, M., Guo, Y.B., 2017. Microstructure evolution characteristics of Inconel 625 alloy from selective laser melting to heat treatment. Mater. Sci. Eng. A 705, 20–31. https://doi.org/10.1016/j.msea.2017.08.058.

Li, Z., Cui, Y., Yan, W., Zhang, D., Fang, Y., Chen, Y., Yu, Q., Wang, G., Ouyang, H., Fan, C., Guo, Q., Xiong, D.-B., Jin, S., Sha, G., Ghoniem, N., Zhang, Z., Wang, Y.M., 2021. Enhanced strengthening and hardening via self-stabilized dislocation network in additively manufactured metals. Mater. Today 50, 79–88. https://doi.org/10.1016/j.mattod.2021.06.002.

Liu, Q., Wang, Y., Zheng, H., Tang, K., Ding, L., Li, H., Gong, S., 2016. Microstructure and mechanical properties of LMD-SLM hybrid forming Ti6Al4V alloy. Mater. Sci. Eng. A 660, 24–33. https://doi.org/10.1016/j.msea.2016.02.069.

Ma, D., Stoica, A.D., Wang, Z., Beese, A.M., 2017. Crystallographic texture in an additively manufactured nickel-base superalloy. Mater. Sci. Eng. A 684, 47–53. https://doi.org/10.1016/j.msea.2016.12.028.

Marchese, G., Garmendia Colera, X., Calignano, F., Lorusso, M., Biamino, S., Minetola, P., Manfredi, D., 2017. Characterization and comparison of inconel 625 processed by selective laser melting and laser metal deposition. Adv. Eng. Mater. 19, 1–9. https://doi.org/10.1002/adem.201600635.

Marchese, G., Lorusso, M., Parizia, S., Bassini, E., Lee, J.W., Calignano, F., Manfredi, D., Terner, M., Hong, H.U., Ugues, D., Lombardi, M., Biamino, S., 2018. Influence of heat treatments on microstructure evolution and mechanical properties of Inconel 625 processed by laser powder bed fusion. Mater. Sci. Eng. A 729, 64–75. https://doi.org/10.1016/j.msea.2018.05.044.

Marchese, G., Parizia, S., Rashidi, M., Saboori, A., Manfredi, D., Ugues, D., Lombardi, M., Hryha, E., Biamino, S., 2020. The role of texturing and microstructure evolution on the tensile behavior of heat-treated Inconel 625 produced via laser powder bed fusion. Mater. Sci. Eng. A 769, 138500. https://doi.org/10.1016/j.msea.2019.138500.

Oh, W.J., Lee, W.J., Kim, M.S., Jeon, J.B., Shim, D.S., 2019. Repairing additive-manufactured 316L stainless steel using direct energy deposition. Opt. Laser Technol. 117, 6–17. https://doi.org/10.1016/j.optlastec.2019.04.012.

Poulin, J., Brailovski, V., Terriault, P., 2018. Long fatigue crack propagation behavior of Inconel 625 processed by laser powder bed fusion: Influence of build orientation and post-processing conditions. Int. J. Fatigue 116, 634–647. https://doi.org/10.1016/j.ijfatigue.2018.07.008.

Qin, L.Y., Men, J.H., Zhang, L.S., Zhao, S., Li, C.F., Yang, G., Wang, W., 2019. Microstructure homogenizations of Ti-6Al-4V alloy manufactured by hybrid selective laser melting and laser deposition manufacturing. Mater. Sci. Eng. A 759, 404–414. https://doi.org/10.1016/j.msea.2019.05.049.

Sánchez Camargo, M.C., 2019. Mechanical Multi-scale Characterization of Metallic Materials by Nanoindentation Test.

Sangid, M.D., Sehitoglu, H., Maier, H.J., Niendorf, T., 2010. Grain boundary characterization and energetics of superalloys. Mater. Sci. Eng. A 527, 7115–7125. https://doi.org/10.1016/j.msea.2010.07.062.

Sateesh, N.H., Kumar, G.C.M., Prasad, K., S, C.K., Vinod, A.R., 2014. Microstructure and mechanical characterization of laser sintered inconel-625 superalloy. Procedia Mater. Sci. 5, 772–779. https://doi.org/10.1016/j.mspro.2014.07.327.

Sealy, M.P., Madireddy, G., Williams, R.E., Rao, P., Toursangsaraki, M., 2018. Hybrid processes in additive manufacturing. J. Manuf. Sci. Eng. 140. https://doi.org/10.1115/1.4038644.

Soffel, F., Eisenbarth, D., Hosseini, E., Wegener, K., 2021. Interface strength and mechanical properties of Inconel 718 processed sequentially by casting, milling, and direct metal deposition. J. Mater. Process. Technol. 291, 117021 https://doi.org/10.1016/j.jmatprotec.2020.117021.

Voisin, T., Forien, J.B., Perron, A., Aubry, S., Bertin, N., Samanta, A., Baker, A., Wang, Y. M., 2021. New insights on cellular structures strengthening mechanisms and thermal stability of an austenitic stainless steel fabricated by laser powder-bed-fusion. Acta Mater. 203. https://doi.org/10.1016/j.actamat.2020.11.018.

Webster, S., Lin, H., Carter, F.M., Ehmann, K., Cao, J., 2021. Physical mechanisms in hybrid additive manufacturing: a process design framework. J. Mater. Process. Technol. 291, 117048 https://doi.org/10.1016/j.jmatprotec.2021.117048.